Hybrid Experimental-Numerical Investigation on Plastic Deformation and Ductile Failure of Anisotropic Sheet Metals

Lin WANG

Hefei University, Hefei, 230061, China, E-mail: linw@smu.edu

1. Introduction

Sheet metal is intensively used in modern industries, including the automotive, aerospace, and military industries due to its high strength-to-weight ratio. Deep knowledges of its plastic deformation and ductile failure are essentially necessary for precise metal forming. Performing full-scale experiment is physically important to understand the plastic deformation and ductile failure behaviours of sheet metal structures, but generally expensive and time consuming. Finite element modelling, alternatively, provides an effective numerical tool to investigate these processes of typical structure materials, if fully represented and accurately realized.

Ductile failure of sheet metal is a very complex physical process characterized as micro-scale void nucleation, growth and ultimate macro-scale crack formation. The Gurson's model takes void volume fraction as internal variable, and assumes that fracture would occur once reaching its threshold value [1]. Due to its effectiveness, the Gurson's model is repeatedly modified to describe the ductile failure phenomenon of plastic metals [2]. However, the parameters embedded in micromechanical models should be well-calibrated, which might be inherently non-unique or even not robust since different parameter combinations appear to capture the softening behaviours of materials or structures [3, 4].

Simpler phenomenological ductile failure models, alternatively, are developed without consideration of micro scale process [5]. It is experimentally found that the ductile damage of sheet metals accumulates in an accelerative way: initially at a very slow rate and then at a much faster pace near the crack initiation and then progress rapidly to completely material separation [4, 6, 7]. It is therefore suitable to describe the ductile failure of metal materials by weighted functions of accumulated plastic strain, stress tensor or other variables [5, 8]. The applicability and validity of such models have been well discussed in works [3, 5, 8-13].

In this present work, we aim to study the plastic deformation and ductile failure of two anisotropic sheet metals by employing hybrid experimental-numerical analysis. U-notched tensile specimen of AISI 1018 low carbon steel and C260 Cu-Zn brass were fabricated and stretched to complete fracture under tension. Via the digital image correlation (DIC) technique, the development of full-filed plastic deformation was measured from specimen surface. Three-dimensional finite element modelling was performed to simulate the material behaviours of sheet metal under tension. The predicted results in global material response, local strain distribution and ductile failure were compared with experimental measurements for effectiveness assessment.

2. Experiment

Attention is focused on notched tensile specimen made of cold-rolled thin sheet metal (low carbon steel, C260 Cu-Zn brass). The specimen is 25.4 wide and 1.50 mm thick with axial loading direction aligned with the rolling direction of sheet metals. Symmetric semi-circle notches of radius 2.5 mm were milled at the appropriate locations centered within the specimen, as shown in Fig. 1. With such geometry, significant large strain is introduced at the notched cross section to trigger the ductile fracture. Slight misalignment of notches is found due to machining error.
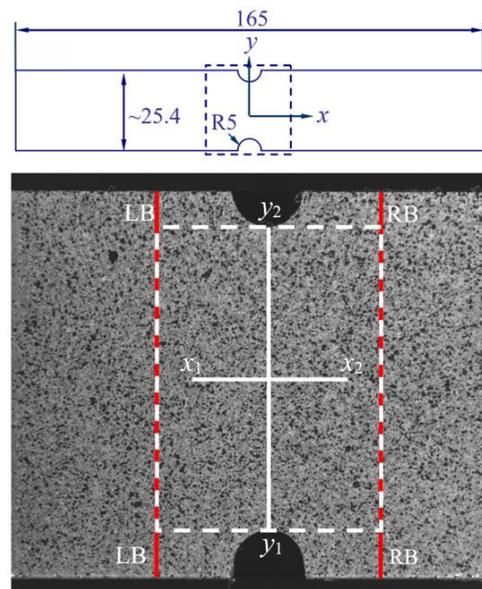

Fig. 1 Specimen geometry and surface decoration

Tension test of notched specimen was conducted on a 5582 Instron test machine. The specimen was stretched to complete fracture at constant displacement loading speed of 1mm/min. One of specimen surfaces was decorated with fine black-and-white paint spackles to facilitate the DIC measurement. A CCD camera (1280×960 pixels, 8-bit, 2 fps) was employed to captured the image of painted specimen surface during the test. The spatial resolution of digital image is about 30 μm/pixel. The DIC measurement of axial elongation $D(t)$ over 15 mm gage length (see the red lines LB and RB in Fig. 1) was then synchronized in time with the applied axial load $F(t)$ recorded by Instron machine.

3. Numerical simulation

Nonlinear FE modeling of notched specimen under uniaxial tension were performed using ANSYS v12.1.

Eight-node 3D solid element (SOLID185) with full integration and large strain effect was used to discretize the notched specimen. The misalignment of semi-circle notches was considered in finite element model. Exploiting the symmetry of specimen geometry and boundary conditions, one half model was established. Symmetric displacement boundary conditions were imposed on planes z=0. As strain localization and ductile failure progressed, significant rotation of the specimens would often occur [14]. The displacement boundary conditions measured by DIC were applied on the left and right ends.

Sheet metal generally exhibits obvious anisotropy in material behavior due to its crystallographic structure and rolling process. Hill's yield criterion in quadratic form was employed to describe the anisotropy of considered sheet metals [15], given by:

$$F(\sigma_y - \sigma_z)^2 + G(\sigma_z - \sigma_x)^2 + H(\sigma_x - \sigma_y)^2 + \\ + 2L\tau_{yz}^2 + 2M\tau_{xz}^2 + 2N\tau_{xy}^2 = \sigma_0^2, \quad (1)$$

where: σ_0 is the reference yield stress and the parameters F, G, H, L, M, N are dependent on the plastic strain ratio R_0, R_{45} and R_{90}. R_0, R_{45} and R_{90} of brass were 0.77, 0.71 and 1.04, respectively, measured from standard uniaxial tension test using DIC. The corresponding values were experimentally determined as 1.55, 0.97 and 1.23 for steel, respectively.

The elastic moduli of the brass and steel are 130 GPa and 200 GPa, and the 0.2% offset yield stress are measured as 230.1 MPa and 208.2 MPa, respectively. As stress-state diverges from uniaxial tension, the stress-strain curve of sheet metal obtained from standard uniaxial tension tests beyond diffuse neck becomes unreliable. Therefore, the post-necking strain hardening behaviors were extracted by using a local correction factor method based on DIC measured full-filed surface strain with quadratic form of Hill's model [16] and shown in Fig. 2. The calibrated isotropic strain hardening behavior was approximated by at least 40 discrete data points as material parameter inputs.
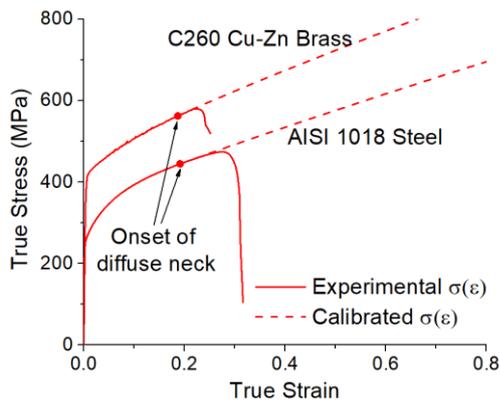

Fig. 2 True stress strain relations of sheet metals

Modeling ductile fracture using the finite element method introduces an artificial length scale and in turn makes the numerical simulation mesh dependent once the strain is localized, which usually occurs before the fracture initiation for ductile materials [17]. Analysis of mesh-size effect was carried on for a notched steel specimen. Three element schemes were considered (Fig. 3): a) coarse mesh with minimum element edge length of l_e=100 μm and n_t=4 elements through half thickness; b) medium mesh with

l_e =50 μm and n_t =6; c) fine mesh with l_e =30 μm and n_t =8. The simulations were run up to the crack initiation point (nominal displacement 2.59 mm). The corresponding force-displacement curves as well as the evolution of equivalent plastic strain of the element on the lower notch root are plotted in Fig. 4. The predicted force displacement relations are approximately mesh independent—no more than 0.3% difference among results from three mesh discretization. All *F-D* curves reasonably match the experimental result. However, a noticeable mesh-size effect on the predicted equivalent plastic strain is detected: the equivalent plastic strains at *D*=2.59 mm computed with the coarse mesh and medium are respectively, 4.8% and 1.1% lower than corresponding results based on fine mesh discretization. In the following, all simulations of notched tensile tests are performed using the fine mesh as l_e =30 μm is about the spatial resolution of captured digital images during tensile tests and the similar element size in numerical simulation of ductile fracture in works [6, 10].
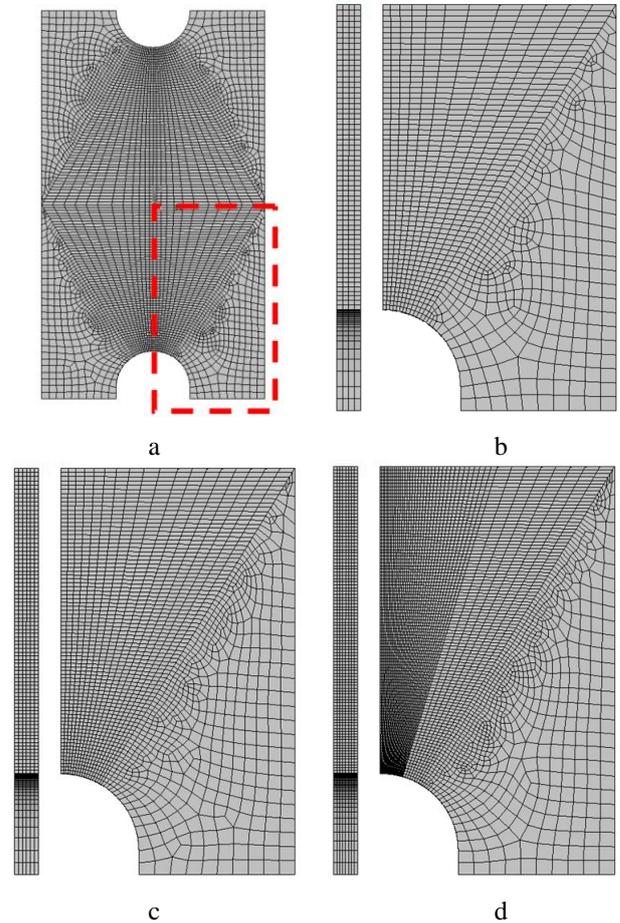

Fig. 3 Finite element discretization of notched specimen a) within region of interest in coarse mesh; b) coarse; c) medium and d) fine meshes in dashed red region

It is well-known that fracture strain ε_f for ductile fracture strongly depends on the stress triaxiality. Stress triaxiality $\sigma^* = \sigma_m / \sigma_{eff}$ is the ratio of the mean stress $\sigma_m = \sigma_{kk}/3$ to effective stress σ_{eff}. If Hill model is applied, the effective stress σ_{eff} is calculated as:

$$\sigma_{eff} = [F(\sigma_y - \sigma_z)^2 + G(\sigma_z - \sigma_x)^2 + \\ + H(\sigma_x - \sigma_y)^2 + 2L\tau_{yz}^2 + 2M\tau_{xz}^2 + 2N\tau_{xy}^2]^{0.5}. \quad (2)$$

When using Hill's potential, the equivalent plastic strain is obtained as following:

$$\varepsilon_{eqv}^{pl} = \int_0^t \frac{\sigma:\dot{\varepsilon}^{pl}}{\sigma_{eff}}\mathrm{d}t. \tag{3}$$
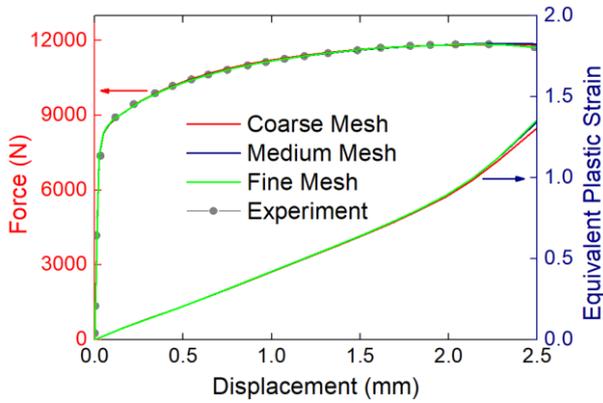

Fig. 4 Effect of element size on the predicted force and equivalent plastic strain versus displacement curves

Although detailed expressions differ slightly from stress triaxiality based failure models, the dependence of ε_f on the stress triaxiality σ^* can be modelled using an exponential function $\varepsilon_f \sim exp(-\alpha\sigma^*)$ [3], where α is a material related constant. Element death technique in ANSYS was employed to simulate the crack evolution. When the equivalent plastic strain ε_{eqv}^{pl} in any element meet the critical value ε_f, the element will be deactivated. A deactivated element remains in the model but contributes a near-zero stiffness to the overall matrix. Any solution-dependent state variables (such as stress, plastic strain, etc.) are set to zero. A restart analysis was carried out to re-equilibrate the finite element solution to make sure no more element exceed the fracture criterion under the same loading condition. Then the displacement boundary conditions were then increased by small increment and such procedures are repeated until the complete fracture. The strain rate was assumed varying in a narrow range, so no strain rate effect was considered.

4. Results and discussions

4.1. Experimental results

The applied force versus displacement relations of notched specimens and captured images during test are plotted in Fig. 5. The solid, open circles and the cross symbol indicate the corresponding points of peak load, crack initiation and load step just prior to complete fracture. The crack initiation point is defined once detectable crack on specimen surface is observed from captured images or the force-displacement relations beyond peak load significantly changes its slope. The global force-displacement relations of three specimens for each material are almost coincident before the crack initiation point. The variations reflect the specimen differences in geometry and embed damage.

For notched brass and steel specimens, the crack initiates from one notch, and gradually propagate to the opposite notch. During this process, new crack might initiate from the other notch, such as the selected brass specimen. The crack length accumulates in an accelerative manner. It took about 50 sec for crack to propagate 10.9 mm through brass specimen, while 130 sec to propagate around 10.3 mm for steel specimen. Then the crack rapidly passed through the remaining material to complete fracture in less than half second. High speed camera is needed to monitor the crack propagation in this latter stage.
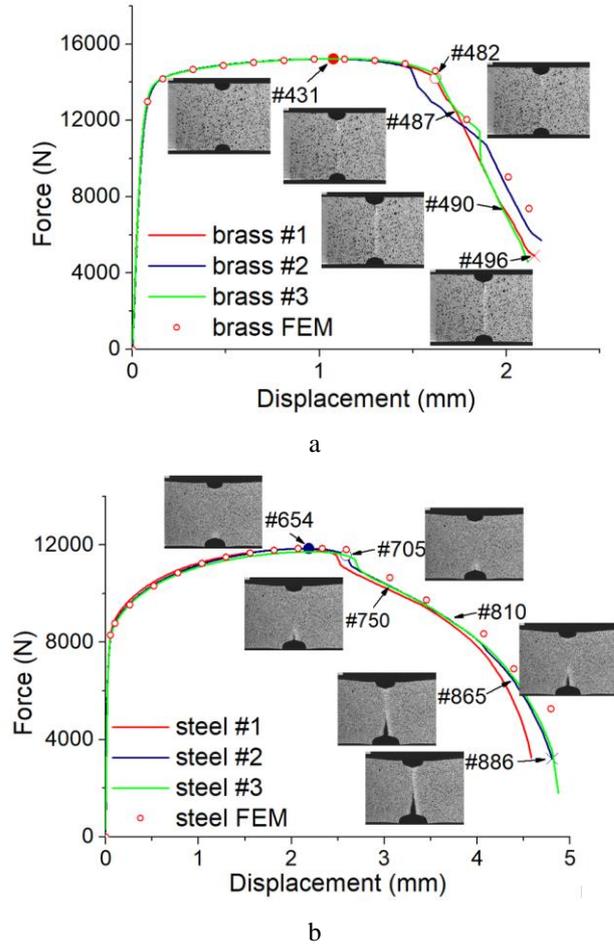

a

b

Fig. 5 Experimental and numerical predicted *F-D* relations for notched specimen made of a) brass and b) steel

The cumulative surface strain of selected notched brass and steel specimens at peak load and crack initiation points were measured within the centered 20 mm×15 mm area (dashed rectangle in Fig. 1) using full-field digital image correlation technique, and shown in Figs. 6 and 7. A subset of 30×30 pixels (900 μm×900 μm) and a grid spacing of 10 pixels (300 μm) in both axial and transverse directions were used in the digital image correlation analysis. The error level for the local axial strain measurements was estimated to be about ±0.05% or less per the quality of experimentally acquired digital images of each test [18]. Due to the notched configuration, the axial strain ε_x at the notches is significantly larger than that in the middle region of specimen. The contour of strain distribution is not symmetric due to the misalignment of notches.

For selected brass specimen, the axial strain ε_x is no larger than 0.05 over most of the specimen surface except the region of the minimum cross section (Fig. 6). The axial strain achieves its maximum as 0.43 and 0.72 at the upper notch at peak load and crack initiation points, respectively. A narrow band of axial strain is formed at the minimum cross section at crack initiation point. The axial strain ε_x in this minimum cross section varies between 0.07 and 0.43 at

the peak load, and from 0.18 to 0.72 at the crack initiation point. The maximum transverse strain ε_y is about -0.13, also

achieving at the top notch. The transverse strain over much specimen surface is quite small.
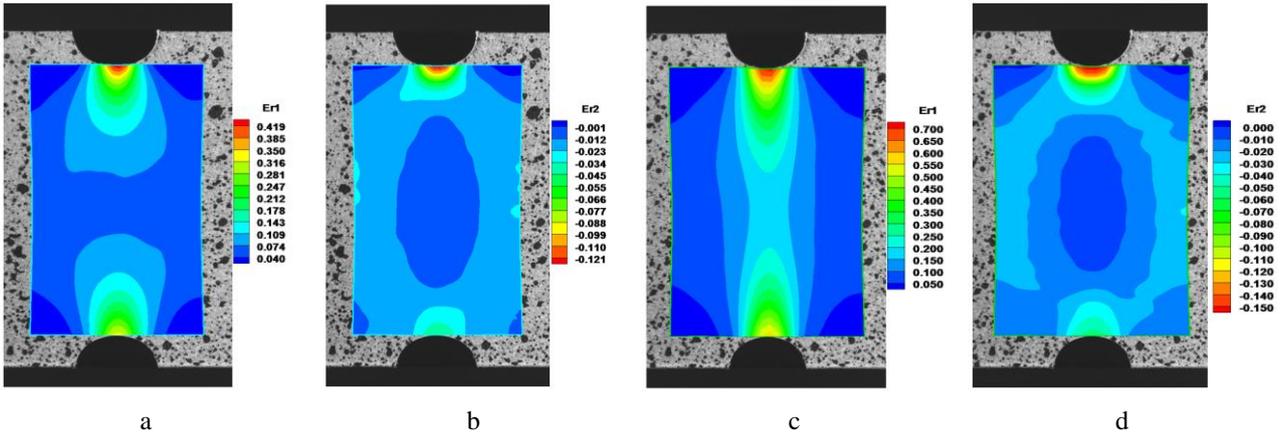

a   b   c   d

Fig. 6 DIC measured contours of a) axial; b) transverse strain at peak load; c) axial; d) transverse strain at crack initiation point of notched brass specimen #1
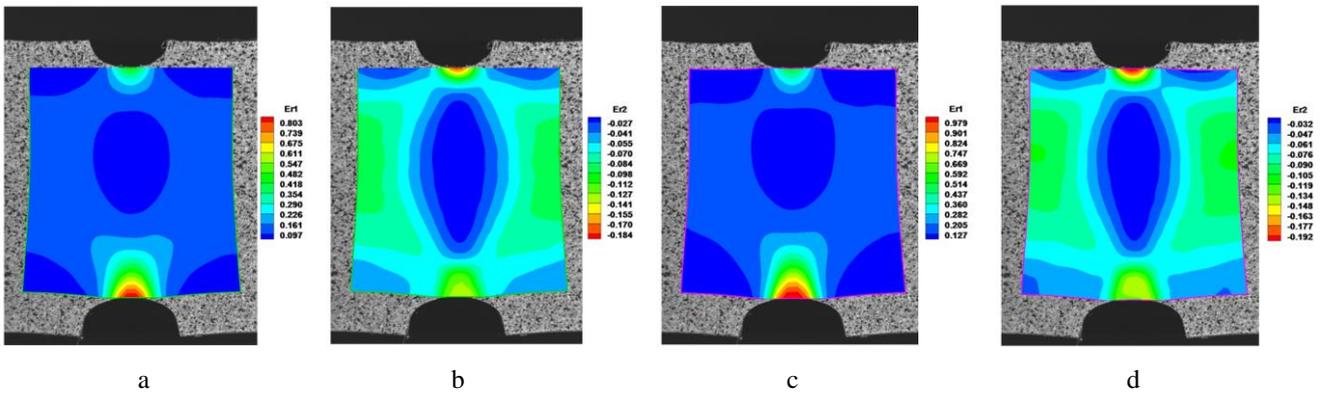

a   b   c   d

Fig. 7 DIC measured contours of a) axial; b) transverse strain at peak load; c) axial; d) transverse strain at crack initiation point of notched steel specimen #2

The maximum axial strain ε_x are 0.78 and 0.99 for selected steel specimen at the bottom notch at peak load and crack initiation points, respectively (see Fig. 7). Differing from notched brass specimens, no narrow band of axial strain ε_x is formed in the minimum cross section with the increasing displacement from peak load to crack initiation point. The variation of axial strain ε_x along the minimum cross section is within the range from 0.06 to 0.78 at peak load, and 0.07 to 0.99 at crack initiation point. The transverse strain ε_y is about -0.02 over the specimen surface except the area neighboring notches. Interestingly, the transverse strain ε_y achieves its maximum as -0.20 at the upper notch, other than the lower notch where the maximum axial strain ε_x is achieved.

4.2. Numerical results

The predicted force versus displacement relations of selected notched brass and steel specimens are compared with experimental results in Fig. 5. As shown in Fig. 5, the predicted global force-displacement relations till the crack initiation point agree well with the experimental measurements. Beyond the crack initiation point, detectable discrepancy in curves is observed between experimental and numerical results. The predicted surface strain contours at peak load and crack initiation points are shown in Figs. 8 and 9. The basic features of strain distributions are successfully captured as compared with experimental results in Figs. 6

and 7. Differing from the experimental measurement, the predicted transverse strain of steel specimen achieving its minimum at the bottom notch, the same location where maximum axial strain achieves.

The variation of axial strain ε_x and transverse strain ε_y along the lines y_1-y_2 and x_1-x_2 is also compared with experimental measurement at the crack initiation point, as shown in Fig. 10. The predicted axial strain ε_x of brass closely approximate the experimental measurements along the major portion of y_1-y_2 line, however, tender to be overestimated neighboring the notches. The single peak of axial strain ε_x along x_1-x_2 is predicted but slightly underestimate. Similarly, the FE modelling of steel specimen also capture the major feature of axial strain ε_x within the minimum cross-section. This discrepancy in maximum axial strain could be as high as 0.32 at the bottom notch of steel. Different from brass, the notched steel specimen achieved its minimal value in axial strain ε_x in the middle of x_1-x_2 line. For both specimens, the discrepancy of transverse strain ε_y as minor strain between numerical and experimental results along lines x_1-x_2 and y_1-y_2 is relatively small.

Though the major features of surface strain variation along selected lines are captured, quantitative difference in surface strain is also detected. First, the post-necking strain hardening of sheet metals calibrated by the local correction factor method may fail to describe the material behavior in lager strain due to DIC measurement limit. Also, the non-quadratic other than quadratic form Hill model may
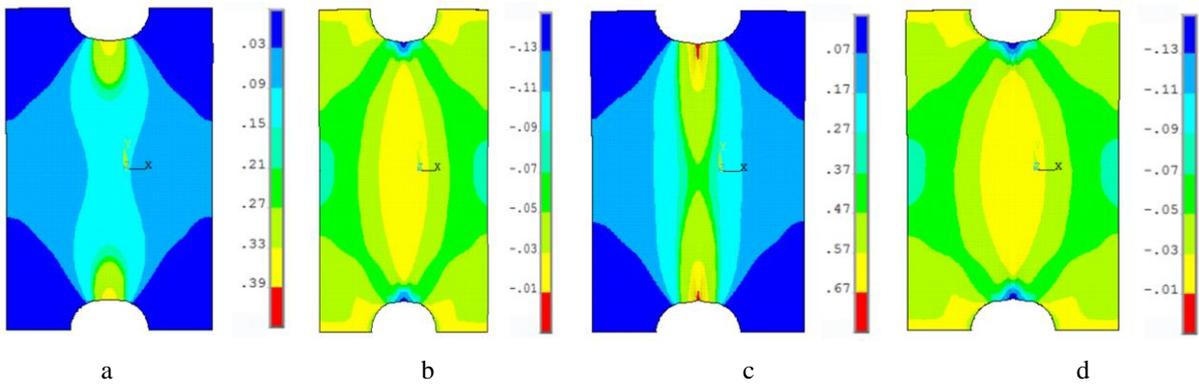
Fig. 8 Numerical predicted contours of a) axial; b) transverse strain at peak load; c) axial; d) transverse strain at crack initiation point of notched brass specimen
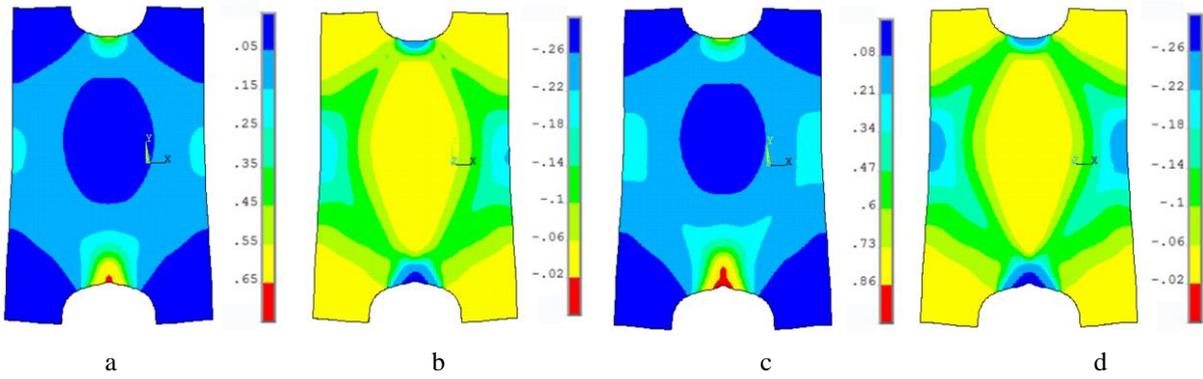

Fig. 9 Numerical predicted contours of a) axial; b) transverse strain at peak load; c) axial; d) transverse strain at crack initiation point of notched steel specimen
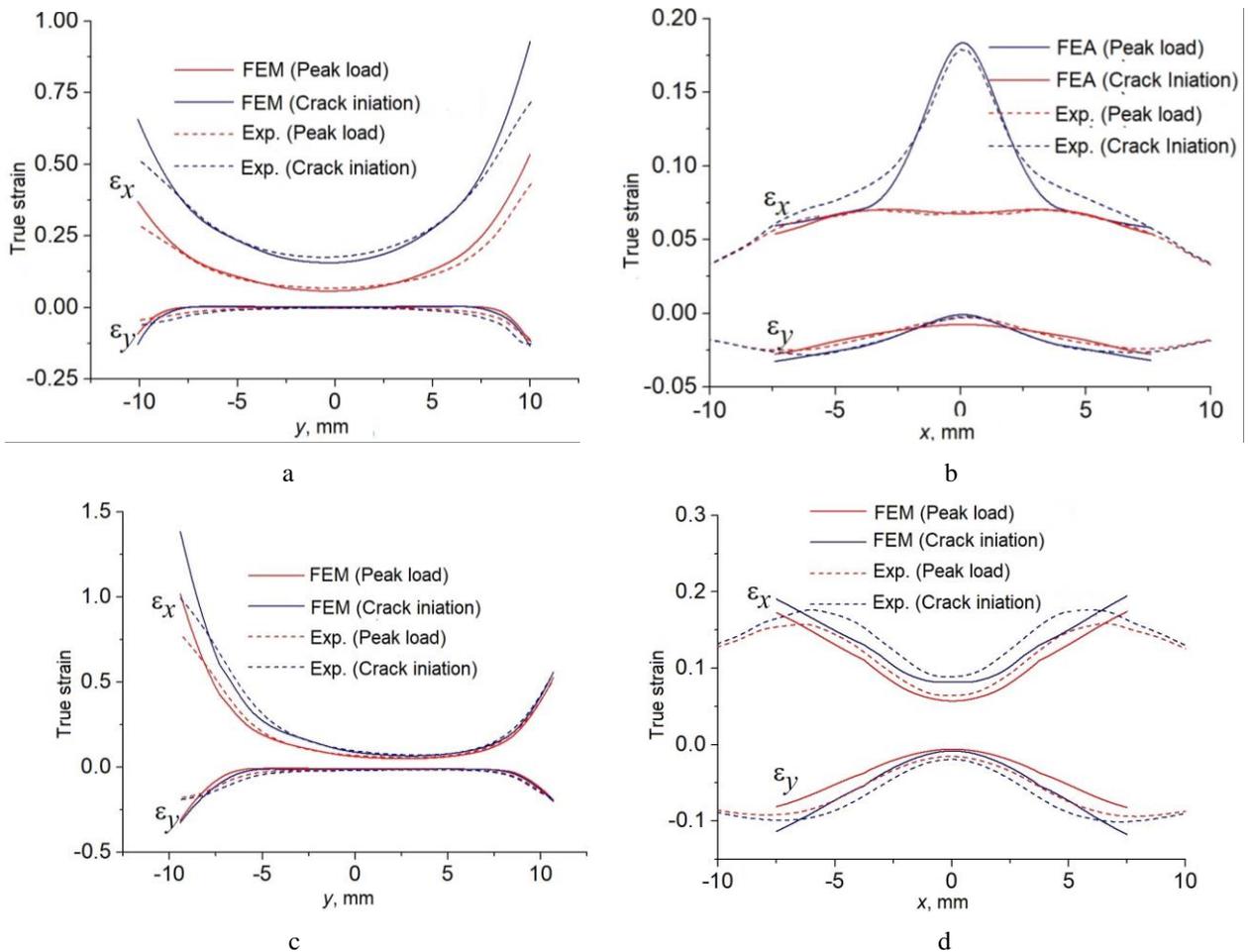

Fig. 10 Strain variation along a) x_1-x_2; b) y_1-y_2 of notched brass, along c) x_1-x_2; d) y_1-y_2 of notched steel

be better to describe the sheet metals under consideration in this work, but special subroutines are need to be implemented into commercial finite element programs. Our previous study already proves that the form of Hill model and the plastic strain ratio would further affect the post-necking strain hardening of sheet metals [16]. Finally, current digital images resolution limits the DIC technique for surface strain measurement at the very later stage of deformation in smaller size scale, while the local strain prior to final failure is reported to be quite high at the level of a few grains [12].

Finite element analysis in above section helps us to figure out the fracture strain at current element size. Fig. 11 shows the equivalent plastic strain evolution as a function of the stress triaxiality of elements on the notch where crack initiates. The red dashed line depicts the evolution at the center in thickness direction, while the navy line shows the evolution on specimen surface. The difference in stress and strain state at the specimen surface and mid-plane in Fig. 11 shows a clear gradient along the thickness direction [11]. The relatively higher triaxiality indicate that the stress state in the mid-plane diverges from plane stress state caused by localized necking. The equivalent plastic strains of specimen surface and mid-plane at crack initiation point are 1.00 and 1.13 for brass, 1.18 and 1.31 for steel, respectively. The critical fracture strain in constant equivalent plastic strains are thus set as 0.9 and 1.1 for brass and steel respectively to mimic the crack propagation considering the small variation in triaxiality.

Fig. 12 gives the crack propagation of notched brass specimen. Two cracks initiate from both notches in numerical prediction at selected displacement loadings of image #487. The crack length is respectively, 2.3 and 1.1 mm for upper and lower cracks. There is just one crack observed from captured images starting from the upper notch with crack length of 2.0 mm. The captured images #490 and #496 verify the two cracks predicted by finite element analysis. The crack length is 5.6 and 4.1 mm, respectively for upper and lower cracks measured from image #490, and 6.5 and 4.3 mm from image #496. The predicted crack length of upper crack is 5.2 and 6.3 mm at displacement loadings corresponding to image #490 and #496. The bottom crack increases from 3.8 mm to 4.0 mm at these two displacement loadings.
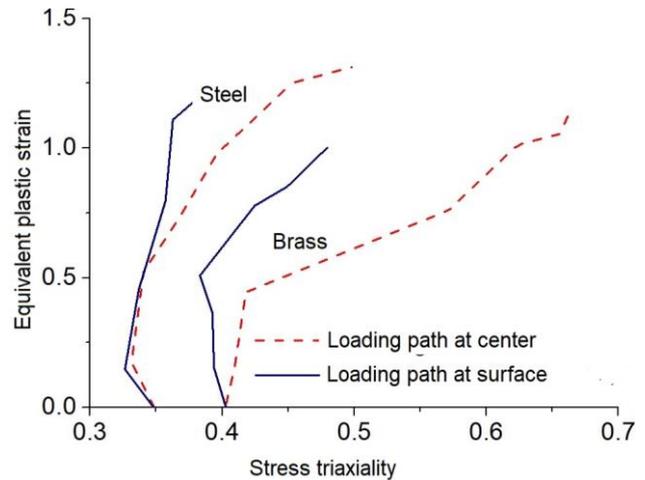

Fig. 11 Loading path of a) brass; b) steel at the notched edge where crack initiates
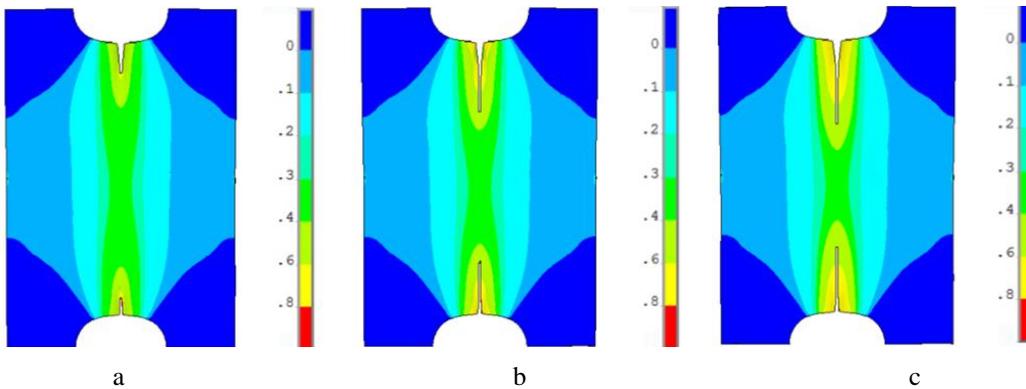

Fig. 12 Predicted crack propagation of notched brass at load step a) #487, b) #490 and c) #496

Fig. 13 plots the predicted crack evolution of steel specimen. The crack lengths in numerical prediction are 2.5, 4.2, and 7.6 mm, while the experimental measurements from corresponding captured image #750, #810, #865 are respectively 2.3, 4.4 and 8.0 mm. At the displacement of image #886 (the last image prior to completely fracture), the numerical simulation shows another crack initiated from the upper notch, though cannot be observed from captured image. The length of bottom crack is 9.6 mm, and the experimental results is about 10.1 mm. In general, the crack evolution of notched sheet metals is effectively simulated by using a critical effective plastic strain to failure model. Mesh-size effect is an important issue for failure analysis of materials and structures [19]. To analyse the dependency of critical value of equivalent plastic strain ε_f on the mesh-size, numerical simulation of failure process for brass and steel specimens was performed based on coarse, medium and fine element discretization. The critical value of equivalent plastic value ε_f was identified if the discrepancy in crack length between experimental and numerical measurements is smaller than 1mm at the displacement loading step just prior to complete fracture. The results indicate that the critical value of equivalent plastic strain ε_f decays with increasing minimum length of element edge [19]. The variations in critical plastic are about 0.2 and 0.25 for brass and steel, respectively, based on coarse and fine mesh discretization. Non-local, higher-order plasticity models are reported to effectively relief or even eliminate the mesh sensitivity [17, 20].
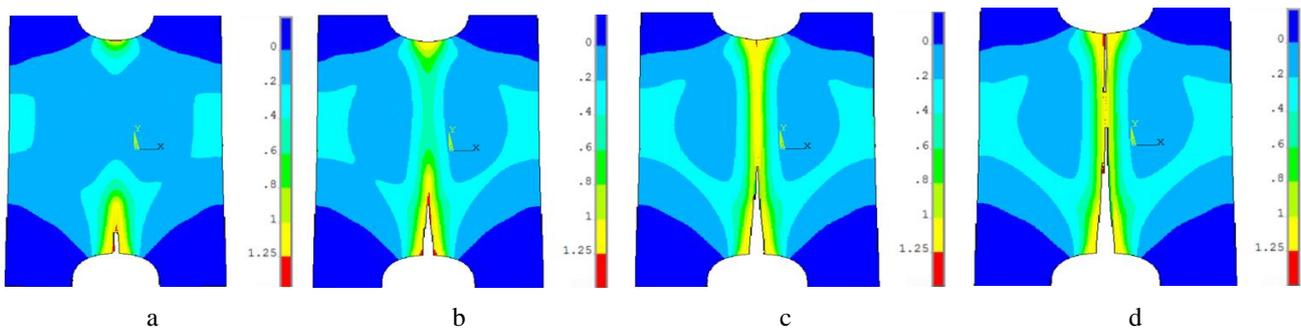
Fig. 13 Predicted crack propagation of notched steel at load step a) #750; b) #810; c) #865; d) #886

5. Conclusions

The plastic deformation and failure process of U-notched sheet metals under tension were studied by using a hybrid experimental-numerical analysis. DIC technique was applied to obtain the full-field surface strain. Three-dimensional finite element modelling using Hill model and effective strain-to-failure criterion was performed to mimic the experimental process. The main conclusions are:

1. The three-dimensional finite element modelling with anisotropic quadratic Hill yield function and identified isotropic post-necking strain hardening behavior from experiment are found effectively predict the plastic deformation of sheet metal under test by comparing with experimental observations.

2. Critical effective strain of two sheet metals dependent on stress triaxiality were identified based on numerical simulation. The predicted fracture process of notched sheet metals using effective strain-to-failure model agrees well with experimental results.

3. Although the numerical simulations with three different meshes provide the same overall force-displacement response, the predicted strain distribution and the identified critical effective plastic strain are found sensitive to element size.

Acknowledgement

References

1. **Gurson, A. L.** 1977. Continuum theory of ductile rupture by void nucleation and growth. Part I: Yield criteria and flow rules for porous ductile media. J. Eng. Mater. Technol. 99: 2–15.
   https://doi.org/10.1115/1.3443401.

2. **Lassance, D.; Fabrègue, D.; Delannay, F.; Pardoen, T.** 2007. Micromechanics of room and high temperature fracture in 6xxx Al alloys, Prog. Mater. Sci. 52(1): 62–129.
   https://doi.org/10.1016/j.pmatsci.2006.06.001.

3. **Oh, C. S.; Kim, N. H.; Kim, Y. J.; Baek, J. H.; Kim, Y. P.; Kim, W. S.** 2011. A finite element ductile failure simulation method using stress-modified fracture strain model, Eng. Fract. Mech. 78: 124-137.
   https://doi.org/10.1016/j.engfracmech.2010.10.004.

4. **Ghahremaninezhad, A.; Ravi-Chandar, K.** 2012. Ductile failure behavior of polycrystalline Al 6061–T6, Int. J. Fract. 174:177–202.
   https://doi.org/10.1007/s10704-012-9689-z.

5. **Wierzbicki, T.; Bao, Y.; Lee, Y. W.; Bai, Y.** 2005. Calibration and evaluation of seven fracture models, Int. J. Mech. Sci. 47(4–5): 719–743.
   https://doi.org/10.1016/j.ijmecsci.2005.03.003.

6. **Xue, L.; Wierzbicki, T.** 2008. Ductile fracture initiation and propagation modeling using damage plasticity theory, Eng. Fract. Mech. 75: 3276-3293.
   https://doi.org/10.1016/j.engfracmech.2007.08.012.

7. **Ghahremaninezhad, A.; Ravi-Chandar, K.** 2013. Ductile failure behavior of polycrystalline Al 6061-T6 under shear dominant loading, Int. J. Fract. 180:23–39.
   https://doi.org/10.1007/s10704-012-9793-0.

8. **Dunand, M.; Mohr, D. 2011.** On the predictive capabilities of the shear modified Gurson and themodified Mohr–Coulomb fracture models over a wide range of stress triaxialities and Lode angles, J. Mech. Phys. Solids. 59(7): 1374–1394.
   https://doi.org/10.1016/j.jmps.2011.04.006.

9. **Bai, Y.; Wierzbicki, T.** 2010. Application of extended Mohr–Coulomb criterion to ductile fracture, Int. J. Fract. 161(1): 1–20.
   https://doi.org/10.1007/s10704-009-9422-8.

10. **Luo, M.; Wierzbicki, T.** 2010. Numerical failure analysis of a stretch-bending test on dual-phase steel sheets using a phenomenological fracture model, Int. J. Solids. Struct. 47(22–23): 3084–3102.
    https://doi.org/10.1016/j.ijsolstr.2010.07.010.

11. **Dunand, M.; Mohr, D.** 2010. Hybrid experimental-numerical analysis of basic ductile fracture experiments for sheet metals, Int. J. Solids. Struct. 47(9): 1130–1143.
    https://doi.org/10.1016/j.ijsolstr.2009.12.011.

12. **Gross, A. J.; Ravi-Chandar, K. 2014.** Prediction of ductile fracture using a local strain-to-failure criterion. Int. J. Fract. 186: 69-91.
    https://doi.org/10.1007/s10704-013-9908-2.

13. **Pack, K.; Luo, M.; Wierzbicki, T.** 2014. Sandia fracture challenge: blind prediction and full calibration to enhance fracture predictability. Int. J. Fract. 186: 155-175.
    https://doi.org/10.1007/s10704-013-9923-3.

14. **Jia, S.; Raiser, G. F.; Povirk, G. L.** 2002. Modeling the effects of hole distribution in perforated aluminum sheets I: representative unit cells, Int. J. Solids. Struct. 39: 2517-2532.
    https://doi.org/10.1016/S0020-7683(02)00115-4.

15. **Hill, R.** 1979. Theoretical plasticity of textured aggregates, Math. Proc. Cambridge. 85: 179-191.

https://doi.org/10.1017/S0305004100055596.

16. **Wang, L.; Tong, W.** 2015. Identification of post-necking strain hardening behavior of thin sheet metals from image-based surface strain data in uniaxial tension tests, Int. J. Solids. Struct. 75: 12-31.
https://doi.org/10.1016/j.ijsolstr.2015.04.038.

17. **Brunet, M.; Morestin, F.; Walter-Leberre, H.** 2005. Failure analysis of anisotropic sheet-metals using a non-local plastic damage model, J. Mater. Process. Technol. 170: 457-470.
https://doi.org/10.1016/j.jmatprotec.2005.05.046.

18. **Tong, W.; Yao, H.; Xuan, Y.** 2011. An improved error evaluation in one-dimensional deformation measurements by linear digital image correlation, Exp. Mech. 51(9): 1019-1031.
https://doi.org/10.1007/s11340-010-9423-6.

19. **Li, Y.; Karr, D. G.** 2009. Prediction of ductile fracture in tension by bifurcation, localization, and imperfection analysis, Int. J. Plasticity. 25: 1128-1153.
https://doi.org/10.1016/j.ijplas.2008.07.001.

20. **Fleck, N.A.; Hutchinson, J. W.** 1993. A phenomenological theory for strain gradient effects in plasticity, J. Mech. Phys. Solids. 41(12): 1825-1857.
https://doi.org/10.1016/0022-5096(93)90072-N.

L. Wang

HYBRID EXPERIMENTAL-NUMERICAL ANALYSIS ON PLASTIC DEFORMATION AND DUCTILE FAILURE OF ANISOTROPIC SHEET METALS

S u m m a r y

The plastic deformation and ductile failure behaviours of anisotropic AISI 1018 low carbon steel and C260 Cu-Zn brass under uniaxial tensile loading were investigated. The full-filed surface deformation of U-notched sheet metal was measured by digital image correlation technique. Three-dimensional finite element modelling using Hill model and calibrated post-necking strain hardening curve was performed to obtain the force and strain history till the crack initiation. The crack propagation was numerically simulated employing a strain-to-failure model. The results from computations as global force-displacement relation, local strain distribution and failure process are found in good agreement with experimental observations.

Keywords: plastic deformation, ductile fracture, anisotropic sheet metal, digital image correlation, finite element modelling.